Efficient catalyst-free N2 fixation by water radical cations under ambient conditions

Xiaoping Zhang, Rui Su, Jingling Li, Liping Huang, Wenwen Yang, Konstantin Chingin, Roman Balabin, Jingjing Wang, Xinglei Zhang, Weifeng Zhu, et al.

nature communications

Article

https://doi.org/10.1038/s41467-024-45832-9

Efficient catalyst-free N_2 fixation by water radical cations under ambient conditions

Received: 10 August 2023

Accepted: 5 February 2024

Published online: 20 February 2024

Check for updates

Xiaoping Zhang[1], Rui Su[2,3], Jingling Li[1], Liping Huang[2], Wenwen Yang[1], Konstantin Chingin[2], Roman Balabin[2], Jingjing Wang[2], Xinglei Zhang[1], Weifeng Zhu[2], Keke Huang[3], Shouhua Feng[3] & Huanwen Chen[1,2]

The growth and sustainable development of humanity is heavily dependent upon molecular nitrogen (N_2) fixation. Herein we discover ambient catalyst-free disproportionation of N_2 by water plasma which occurs via the distinctive HONH-$HNOH^{+\bullet}$ intermediate to yield economically valuable nitroxyl (HNO) and hydroxylamine (NH_2OH) products. Calculations suggest that the reaction is prompted by the coordination of electronically excited N_2 with water dimer radical cation, $(H_2O)_2^{+\bullet}$, in its two-center-three-electron configuration. The reaction products are collected in a 76-needle array discharge reactor with product yields of 1.14 μg cm^{-2} h^{-1} for NH_2OH and 0.37 μg cm^{-2} h^{-1} for HNO. Potential applications of these compounds are demonstrated to make ammonia (for NH_2OH), as well as to chemically react and convert cysteine, and serve as a neuroprotective agent (for HNO). The conversion of N_2 into HNO and NH_2OH by water plasma could offer great profitability and reduction of polluting emissions, thus giving an entirely look and perspectives to the problem of green N_2 fixation.

Nitrogen is an essential element for all living organisms on our planet. Molecular nitrogen (N_2) accounts for more than 99% of global nitrogen[1] but is chemically stable (N ≡ N bond energy ca. 9.5 eV) and thus cannot be directly utilized unless fixed by alternating its oxidation state into bioavailable forms[2]. The problem of N_2 fixation is one of the most important for sustainable chemistry. Currently, N_2 on Earth is predominantly fixed through geochemical processes such as lightning, biologically by nitrogenases, and industrially through the Haber-Bosch (HB) process[3]. While HB is currently the major industrial process for N_2 fixation to ammonia (NH_3), it is associated with intensive reaction conditions (ca. 100 bar and 500 °C), severe environmental pollution (>1% of the global carbon emission) and high consumption of fossil fuel (1%–2% of global energy consumption). These issues are becoming increasingly crucial for the global sustainable development, and urge alternative strategies for N_2 fixation under mild conditions[4,5]. Extensive research is being done in search of alternative strategies for N_2 fixation, including electrocatalytic[6,7], photocatalytic[8], biological[9], and plasma-based[10] methods, but none of these methods have yet been able to rival the overall performance of HB process with regard to the cost efficiency, scalability and selectivity of N_2 fixation[6,11,12].

Recent studies indicate that the N ≡ N bond can be weakened by accepting electrons from the bonding orbitals of N_2 to the antibonding orbitals and/or donating electrons, which would make its functionalization feasible[13,14]. The weakening of N ≡ N bond could be further promoted through the excitation of N_2 into its triplet state, e.g., by electronic or collisional activation with molecules or ions[15,16]. Recently, we have discovered that abundant radical cations of water clusters, especially in the dimer form, $(H_2O)_2^{+\bullet}$, can be produced by electron stripping from neutral water molecules in a strong electric field of the energy-tunable corona discharge of the pure water vapor at atmospheric pressure[17]. The as-prepared water radical cations showed the high reactivity toward a wide range of volatile molecules, such as benzene, carbon-carbon double bond, acetone, ethyl acetate and dimethyl disulfide, revealing rich chemistry with the ionic and radical characters[17–21].

[1]Jiangxi Key Laboratory for Mass Spectrometry and Instrumentation, East China University of Technology, Nanchang 330013, P. R. China. [2]School of Pharmacy, Jiangxi University of Chinese Medicine, Nanchang 330004, P. R. China. [3]State Key Laboratory of Inorganic Synthesis and Preparative Chemistry, College of Chemistry, Jilin University, Changchun 130012, P. R. China. e-mail: chw8868@gmail.com

In this work, we discovered that, owing to its distinct two-center-three-electron (2c-3e) configuration, $(H_2O)_2^{+\bullet}$ can specifically activate N_2 via the formation of HONH-$HNOH^{+\bullet}$ intermediate to selectively disproportionate it into hydroxylamine (NH_2OH) and nitroxyl (HNO) products under mild ambient conditions and with no catalyst involved. These products are not commonly observed upon N_2 fixation and have high value. NH_2OH is widely used in medicine, textile industry, electronics, chemical synthesis, nuclear industry and other fields[22]. HNO is a valuable material for medical and biology utilities, particularly for biological targets of thiols and metalloproteins in fighting cancer[23]. Importantly, HNO is known for its cardioprotective and neuroprotective effects and is resistant to superoxide scavenging and tolerance development[24]. Overall, the study provides an interesting twist on N_2 fixation in terms of both the approach and the products.

Results and discussion

Disproportionation reaction of N_2 with $(H_2O)_2^{+\bullet}$

In our first experiment, water plasma was generated by discharge of water/argon vapor mixture (Supplementary Fig. 1a). The major ionic species observed by real-time mass spectrometry (MS) detection included protonated water clusters, $(H_2O)_2H^+$ (*m/z* 37) and $(H_2O)_3H^+$ (*m/z* 55), as well as abundant water dimer radical cation, $(H_2O)_2^{+\bullet}$ (*m/z* 36) (Supplementary Fig. 1b), in agreement with previous reports[17–20,25,26]. Remarkably, when neutral N_2 was introduced to intersect with the water plasma ca. 1 cm away from the discharge area (Supplementary Fig. 1c), abundant ions at *m/z* 32 and *m/z* 33 and *m/z* 64 were observed (Supplementary Fig. 1d). This observation indicates that the signals *m/z* 32, *m/z* 33 and *m/z* 64 correspond to the species formed due to the interaction between water plasma and neutral N_2. When N_2 was directly flown into the discharge area together with water vapor through the same channel (Fig. 1a), the same product ions at *m/z* 32 and *m/z* 33 and *m/z* 64 were observed with ca. two-fold higher intensity (Fig. 1b). The higher intensity of product ions in the single-channel configuration is probably due to the higher density of N_2 and water plasma right at the end of the electrode than ca. 1 cm away from the end of the electrode (as in the two-channel configuration), which results in higher collision rate between N_2 and water plasma species. Therefore, the single-channel configuration was applied in the subsequent scale up experiments to obtain higher yields of products. We tentatively assigned these signals to $HNOH^+$ (*m/z* 32), $NH_2OH^{+\bullet}$ (*m/z* 33) and HONH-$HNOH^{+\bullet}$ (*m/z* 64), respectively. We speculated that these ionic species could be derived through the reaction between $(H_2O)_2^{+\bullet}$ and N_2. To verify this assumption, $(H_2O)_2^{+\bullet}$ ions (*m/z* 36) formed in the water plasma were selectively isolated in the ion trap by radio frequency (RF) field with peak-to-peak voltage of ~ 100 V in the presence of neutral N_2 gas, which was directly introduced into the ion trap (Fig. 1c). This experiments design allowed us to specifically probe the intrinsic reactivity of N_2 toward $(H_2O)_2^{+\bullet}$ in vacuum without any chemical interference. When the trapped $(H_2O)_2^{+\bullet}$ ions were activated by RF field, the product signals were unambiguously observed at *m/z* 18 (elimination of H_2O from $(H_2O)_2^{+\bullet}$), *m/z* 19 (elimination of $^{\bullet}OH$ from $(H_2O)_2^{+\bullet}$), *m/z* 33 ($NH_2OH^{+\bullet}$), *m/z* 51 ($NH_2OH^{+\bullet}$ plus H_2O), *m/z* 55 ($(H_2O)_3H^+$) and *m/z* 64 (HONH-$HNOH^{+\bullet}$) (Fig. 1d). These observations confirm the occurrence of reaction between $(H_2O)_2^{+\bullet}$ and N_2. Curiously, the signal of $HNOH^+$ abundantly produced upon the interaction between water plasma and N_2 (*m/z* 32 in Fig. 1b) was almost undetectable when $(H_2O)_2^{+\bullet}$ was activated in the ion trap (Fig. 1d), probably because the HNO was initially created as neutral species. During the interaction between water plasma and N_2, neutral HNO could be easily protonated by other ionic species such as $(H_2O)_2H^+$ (*m/z* 37) to give the protonated signal at *m/z* 32 (Fig. 1b), whereas when produced in the ion trap neutral HNO would be instantly pumped out of the ion trap (maintained at high vacuum of 10^{-5} Torr).

The signal at *m/z* 64 was assigned to HONH-$HNOH^{+\bullet}$ intermediate produced during the reaction between N_2 and $(H_2O)_2^{+\bullet}$.

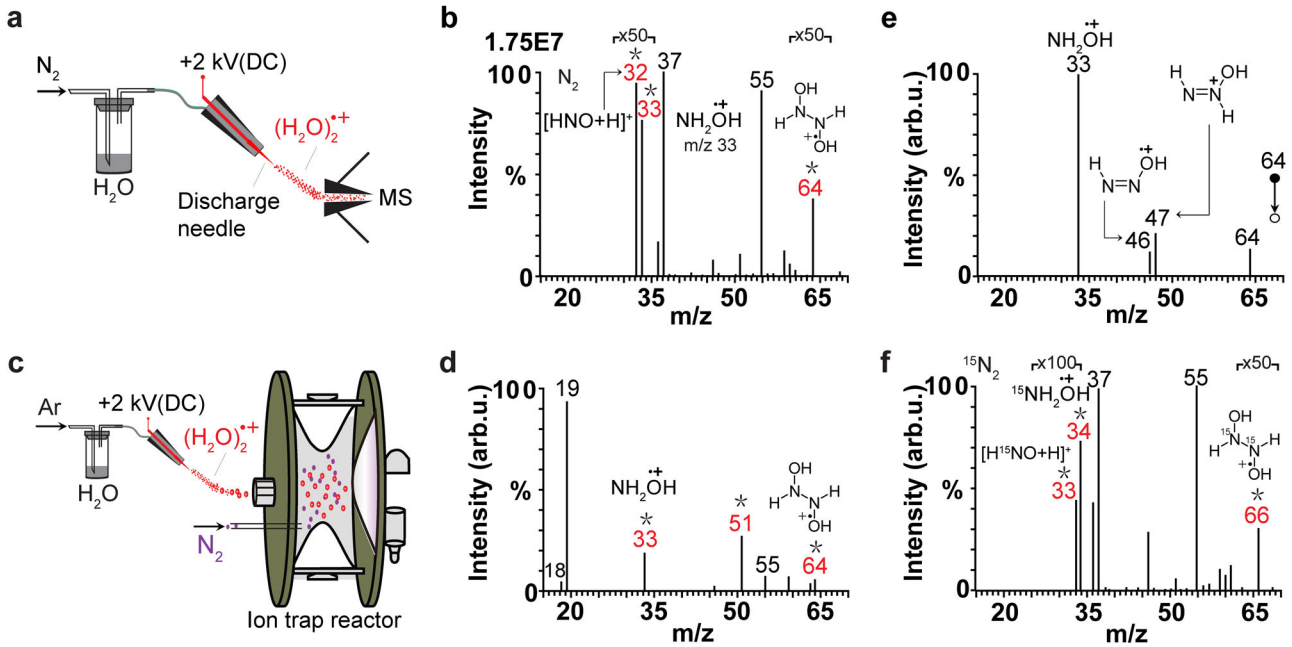

Fig. 1 | Disproportionation reaction of N_2 with water dimer radical cation. **a** Experimental setup to study the interaction of N_2 with water vapor plasma at ambient conditions. Stainless-steel discharge needle was used as electrode. DC: direct current. The figure is adapted with permission from refs. 18,20,21. **b** The corresponding mass spectrum of ionic products in Fig. 1a. Asterisks correspond to the products specific to the reaction between water vapor plasma and N_2. **c** Ion trap reactor applied to study the reaction between N_2 and isolated $(H_2O)_2^{+\bullet}$ (*m/z* 36) in vacuum. The figure is adapted with permission from refs. 18,20,21. **d** The corresponding mass spectrum of ionic products in **c**. Asterisks correspond to the products specific to the reaction between water vapor plasma and N_2. **e** Ionic fragments of the reaction intermediate at *m/z* 64 induced by collisional activation inside the ion trap. **f** Mass spectrum of the ionic species observed during the interaction between water vapor plasma and $^{15}N_2$ ($^{15}N_2$ gas instead of $^{14}N_2$ in **a**). Asterisks correspond to the products specific to the reaction between water vapor plasma and $^{15}N_2$.

https://doi.org/10.1038/s41467-024-45832-9

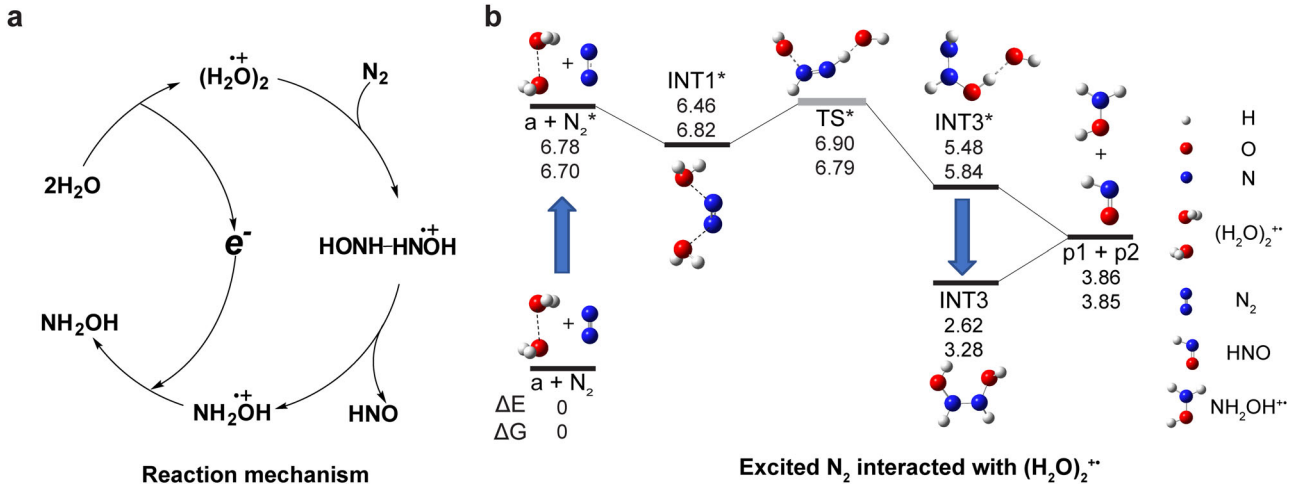

Fig. 2 | Mechanism and calculation results for the reaction of N_2 with $(H_2O)_2^{\bullet+}$. **a** Schematic diagram summarizing a possible mechanism for the reaction of N_2 with $(H_2O)_2^{\bullet+}$. **b** The geometries and energies (in eV at 298 K and 1 atm pressure) of possible molecular and ionic species involved in the disproportionation reaction $N_2 + (H_2O)_2^{\bullet+} \rightarrow NH_2OH^{\bullet+} + HNO$ calculated with CCSD(T) method. Our expected accuracy is 0.04 eV, with the exception of transition state (TS) structure (gray, see Supplementary Note 1). Vertical arrows correspond to the process of electronic excitation/de-excitation. a: $[H_2O{\bullet\bullet\bullet}OH_2]^+$. p1: $NH_2OH^{\bullet+}$. p2: HNO. The atomic coordinates of the optimized computational models are shown in Supplementary Data File.

The chemical assignment of the *m/z* 64 signal to HONH-HNOH$^{\bullet+}$ was supported by collision-induced dissociation (CID) data (Fig. 1e), showing the characteristic fragment at *m/z* 33 corresponding to the elimination of HNO, accompanied by lower-intensity fragments at *m/z* 46 and *m/z* 47 (also discerned in the spectra Fig. 1b), corresponding to the elimination of H_2O and $^{\bullet}OH$ (the dissociation path shown in Supplementary Fig. 1e), respectively. These chemical assignments were further supported by experiments with isotopic substituents (Fig. 1f, Supplementary Fig. 1 f, g). When H_2O in our experiments was replaced by deuterated water, D_2O, the abundant signals at *m/z* 33, *m/z* 34 and *m/z* 35 (Supplementary Fig. 1f) were observed, indicating the formation of $HNOD^+$, $DNOD^+/NH_2OD^{\bullet+}$, and $NHDOD^{\bullet+}$, respectively. Similarly, when N_2 was replaced by $^{15}N_2$, the signals at *m/z* 33 and *m/z* 34 were detected (Fig. 1f), indicating the formation of $H^{15}NOH^+$ and $^{15}NH_2OH^{\bullet+}$, respectively. Interestingly, the HONH-HNOH$^{\bullet+}$-type intermediate was also detected in the experiments with isotopic substitutes: as DOND-DNOD$^{\bullet+}$ (*m/z* 68) for the D_2O experiment (Supplementary Fig. 1f) and as $HO^{15}NH\text{-}H^{15}NOH^{\bullet+}$ (*m/z* 66) for the $^{15}N_2$ experiment (Fig. 1f), respectively. Note that the intermediates labeled with different isotopes showed the identical fragmentation path (Supplementary Fig. 1g). Further reference experiments carried out in our lab indicated that the observed nitrogen disproportionation occurred specifically as the result of reaction between neutral N_2 and $(H_2O)_2^{\bullet+}$: no products could be detected when isolated $N_2^{\bullet+}$ was exposed to neutral water vapor in the ion trap (Supplementary Fig. 1h). Therefore, the spectral data obtained in all the above-mentioned experiments strongly indicate that the observed species correspond to the disproportionation reaction of N_2 with $(H_2O)_2^{\bullet+}$.

Reaction mechanism

Derived from the experimental observations and theoretical calculations (as detailed in Supplementary Data File), a possible reaction pathway for N_2 disproportionation with $(H_2O)_2^{\bullet+}$ is proposed as shown in Fig. 2a. At the first step, neutral H_2O is ionized to form $(H_2O)_2^{\bullet+}$ species[17–20]. Our calculations indicate that N_2 disproportionation with $(H_2O)_2^{\bullet+}$ is thermodynamically not allowed ($\Delta E \approx 3.8$ eV) when N_2 is present in its ground singlet ($X\ ^1\Sigma_g^+$) state (Supplementary Fig. 2) but may occur ($\Delta E \approx -2.9$ eV) when N_2 is present in its more active triplet ($A\ ^3\Sigma_u^+$) state, N_2* (Fig. 2b). It is well known that N_2 is effectively transferred from its singlet state to its triplet state through the collisions with electrons (*e.g.*, in N_2 and CO_2 gas lasers), ions or molecules[15]. It has been shown that, owing to its high molecular symmetry, N_2* exhibits high stability and lives for up to 1.3 s[27], which allows its involvement in chemical reactions, such as the above-mentioned N_2 disproportionation. When the disproportionation of N_2 is carried in water plasma (Fig. 1a) singlet N_2 could be easily activated to triplet N_2* through collisions with high-energy $(H_2O)_2^{\bullet+}$ and other species in water plasma. When the reaction between N_2 and $(H_2O)_2^{\bullet+}$ is carried inside the ion trap, singlet N_2 could be activated to triplet N_2* through collisions with $(H_2O)_2^{\bullet+}$ species activated by RF field (Fig. 1c). Accordingly, no reaction products were observed when $(H_2O)_2^{\bullet+}$ ions were trapped in N_2 gas without activation (Supplementary Fig. 1i). Also, note that, being an electronic transition, N_2 activation to N_2* occurs on a much shorter time scale compared to atomic rearrangements. Therefore, the event of N_2 activation to N_2* and the following association between N_2* and $(H_2O)_2^{\bullet+}$ could occur within a single collision between N_2 and $(H_2O)_2^{\bullet+}$.

In agreement with previous theoretical and experimental reports, our calculations indicate the co-existence of two $(H_2O)_2^{\bullet+}$ configurations, i.e., hydrogen-bonded $[H_3O^+{\bullet\bullet\bullet}OH]$ and $[H_2O{\bullet\bullet\bullet}OH_2]^+$ (+0.3 eV)[17]. Despite the $[H_3O^+{\bullet\bullet\bullet}OH]$ configuration being the global energy minimum for $(H_2O)_2^{\bullet+}$, we could not find a stable intermediate structure for the binding of N_2* with $[H_3O^+{\bullet\bullet\bullet}OH]$. In contrast, we could easily locate a stable intermediate structure for the binding of N_2* with the $[H_2O{\bullet\bullet\bullet}OH_2]^+$ configuration (Fig. 2b). The association of $[H_2O{\bullet\bullet\bullet}OH_2]^+$ configuration with N_2* occurs due to stabilization of the positive charge jointly by the N_2 and the two H_2O moieties (INT1*, Fig. 2b). The INT1* structure is then converted into the excited-state intermediate HONH-HNOH$^{\bullet+}$* (INT3*, $\Delta E = -1.4$ eV, Fig. 2b) by the direct double-proton transfer through an excited transition state (TS*) structure (Fig. 2b, Supplementary Fig. 3). The HONH-HNOH$^{\bullet+}$* intermediate spontaneously and irreversibly dissociates into neutral HNO and cationic $NH_2OH^{\bullet+}$ ($\Delta E = -1.6$ eV, Fig. 2b). In addition to the dissociation channel, HONH-HNOH$^{\bullet+}$* could also relax to its ground state, HONH-HNOH$^{\bullet+}$ (INT3, $\Delta E = -2.8$ eV, Fig. 2b), without dissociation. It is probably through this latter channel that the stable HONH-HNOH$^{\bullet+}$ signal is detected in our experiments (*m/z* 64, Fig. 1b). The HONH-HNOH$^{\bullet+}$ structure could dissociate into HNO and $NH_2OH^{\bullet+}$ by collisional activation ($\Delta E = 1.2$ eV, Fig. 2b), just as observed in the ion trap experiments (Fig. 1d). The $NH_2OH^{\bullet+}$ product can be neutralized to NH_2OH by electron transfer from the environment.

https://doi.org/10.1038/s41467-024-45832-9

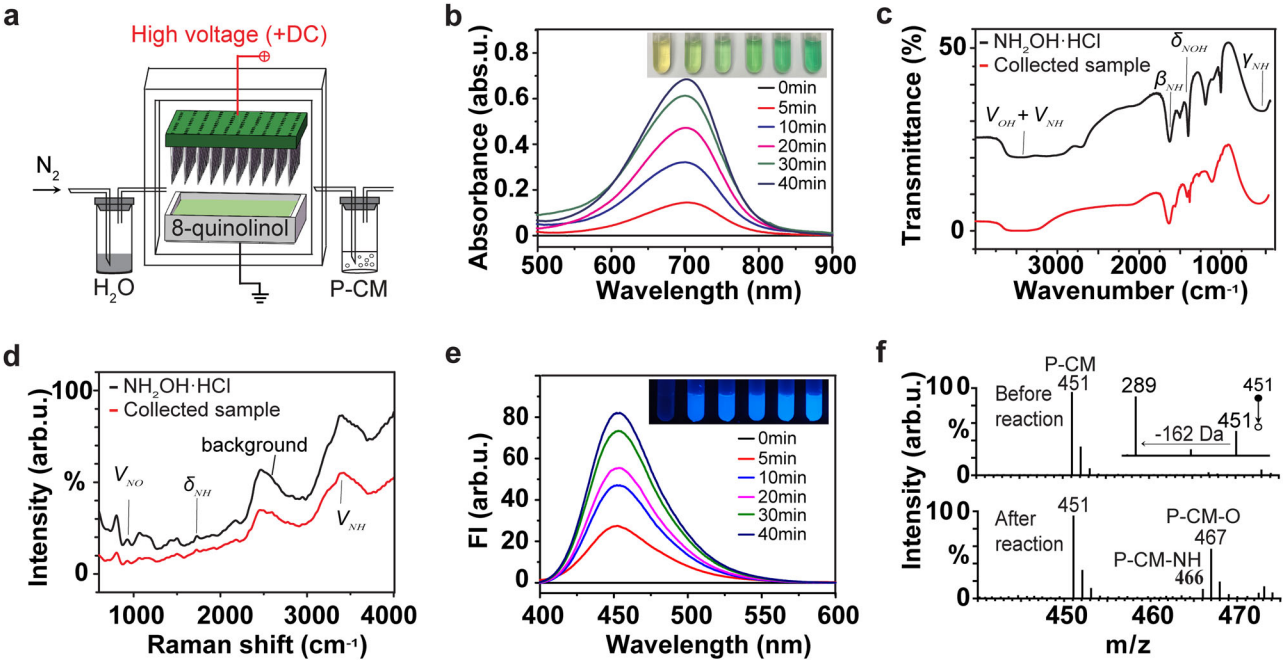

Fig. 3 | Products of ambient disproportionation reaction of N_2 with $(H_2O)_2^{+\bullet}$ characterized by spectral methods. a Schematic illustration of the reaction assembly for scale-up reaction and the collection of reaction products. DC: direct current. The 76 anodes of the array were connected to the same positive terminal of the DC high voltage power. The figure is adapted with permission from refs. 18,20,21. **b** Ultraviolet-visible spectra of indooxine formed through the online reaction of the collected NH_2OH with 8-quinolinol probe at different times of the reaction between N_2 and $(H_2O)_2^{+\bullet}$. **c** Infrared spectra of the collected sample (red) and NH_2OH•HCl standard (black). **d** Raman spectra of the collected sample (red) and NH_2OH•HCl standard (black). **e** Fluorescence spectra of 7-hydroxycoumarin formed through the online reaction of the collected HNO with P-CM probe at different times of the reaction between N_2 and $(H_2O)_2^{+\bullet}$. **f** Mass spectra of P-CM solution before and after collection of the reaction mixture, showing the formation of P-CM aza-ylide (P-CM-NH) and P-CM oxide (P-CM-O) due to the reaction between P-CM and HNO. The inset figure shows the tandem mass spectrum of protonated P-CM at *m/z* 451. P-CM: coumarin-based fluorescent probe.

Overall, it is clear that N_2 fixation by $(H_2O)_2^{+\bullet}$ via HONH-HNOH$^{+\bullet}$ intermediate is mechanistically distinct from the earlier described processes of catalytic nitrogen fixation by molecular hydrogen at a heterogeneous surface[28], in which nitrogen reduction on metal catalyst usually proceeds via N_2H_x-type intermediates ($0 \le x \le 2$). Therefore, this report presents a peculiar mechanism of N_2 fixation.

Scale-up reaction

The disproportionation reaction of N_2 with $(H_2O)_2^{+\bullet}$ was scaled up under ambient conditions using the setup in Fig. 3a, which consisted of an array of 76 needles evenly distributed on a ~ 3.5 × 5.5 cm^2 tungsten plate to generate abundant $(H_2O)_2^{+\bullet}$ and the accessories to collect the NH_2OH and HNO products. We found that NH_2OH was most efficiently collected at the cathode electrode, while HNO was most efficiently collected through the neutral outlet line (Fig. 3a). These observations further support the conclusion that NH_2OH in the reaction was formed in cationic form while HNO was formed in neutral form. Also, these observations enabled special experimental design whereby the HNO and $NH_2OH^{+\bullet}$ products could be spatially separated upon collection: the positively charged $NH_2OH^{+\bullet}$ product is driven by electric field into collection plate at the cathode, while the neutral HNO product is carried with the N_2 stream to the bottle at the upper outlet of the reactor (Fig. 3a). This experimental design effectively prevents the back reaction between HNO with NH_2OH to form N_2 and $2H_2O$. Note that according to our calculations the back reaction between the HNO and NH_2OH products while in the gas phase (e.g., in situ near the discharge area) is hindered by the rather significant energy barrier of ca. 1.4 eV.

Under the optimized experimental conditions, the production of 18.5 μM NH_2OH and 17.7 μM HNO products could be achieved within just 10 min, as quantified by standard spectrophotometric methods (Supplementary Fig. 4, Supplementary Fig. 5). The collected NH_2OH was reacted with an optical probe 8-quinolinol to form indooxine, which was quantified by ultraviolet-visible (UV-Vis) spectroscopy[29]. The signal intensity showed clear correlation with the time of the reaction between N_2 and $(H_2O)_2^{+\bullet}$ (Fig. 3b). The formation of indooxine due to the reaction between NH_2OH and 8-quinolinol was further confirmed by tandem MS experiments through the comparison with indooxine standard (Supplementary Fig. 6a). The formation of NH_2OH product due to the disproportionation reaction between N_2 and $(H_2O)_2^{+\bullet}$ was further validated by infrared and Raman (Fig. 3c, d) spectroscopy of the collected samples.

Similarly, the collected HNO was reacted with a coumarin-based fluorescent probe, called P-CM, to form 7-hydroxycoumarin. The 7-hydroxycoumarin was quantified by fluorescence spectroscopy. The signal intensity showed clear correlation with the time of the reaction between N_2 and $(H_2O)_2^{+\bullet}$ (Fig. 3e). The occurrence of the reaction between P-CM and the HNO product was further confirmed by the detection of other products of the reaction between P-CM and HNO: the P-CM aza-ylide and P-CM oxide (Fig. 3f, Supplementary Fig. 6b), which were in good agreement with the literature data[30]. Note that the preparation and characterization of P-CM is described in the Supplementary Fig. 6c, d.

A series of reference experiments further confirmed the identify of NH_2OH product and its formation by N_2 reduction. No NH_2OH signal was detected either in the blank control setup or in the Ar atmosphere (N_2 was replaced by Ar in Fig. 3a), while clear NH_2OH signal was detected in both the synthetic air atmosphere and pure N_2 atmosphere (Supplementary Fig. 7). The efficiency of NH_2OH product formation in synthetic air was about 50% of that in N_2, which may be due to the lower content of N_2 in the synthetic air as well as due to the influence of O_2. Further, the proton nuclear magnetic resonance (^{1}H NMR) spectrum of the condensate collected in the reaction between N_2 and water plasma displayed a peak at 10 ppm, which matched the peak generated by standard NH_2OH•HCl (Supplementary Fig. 8a). Consistently, the

https://doi.org/10.1038/s41467-024-45832-9

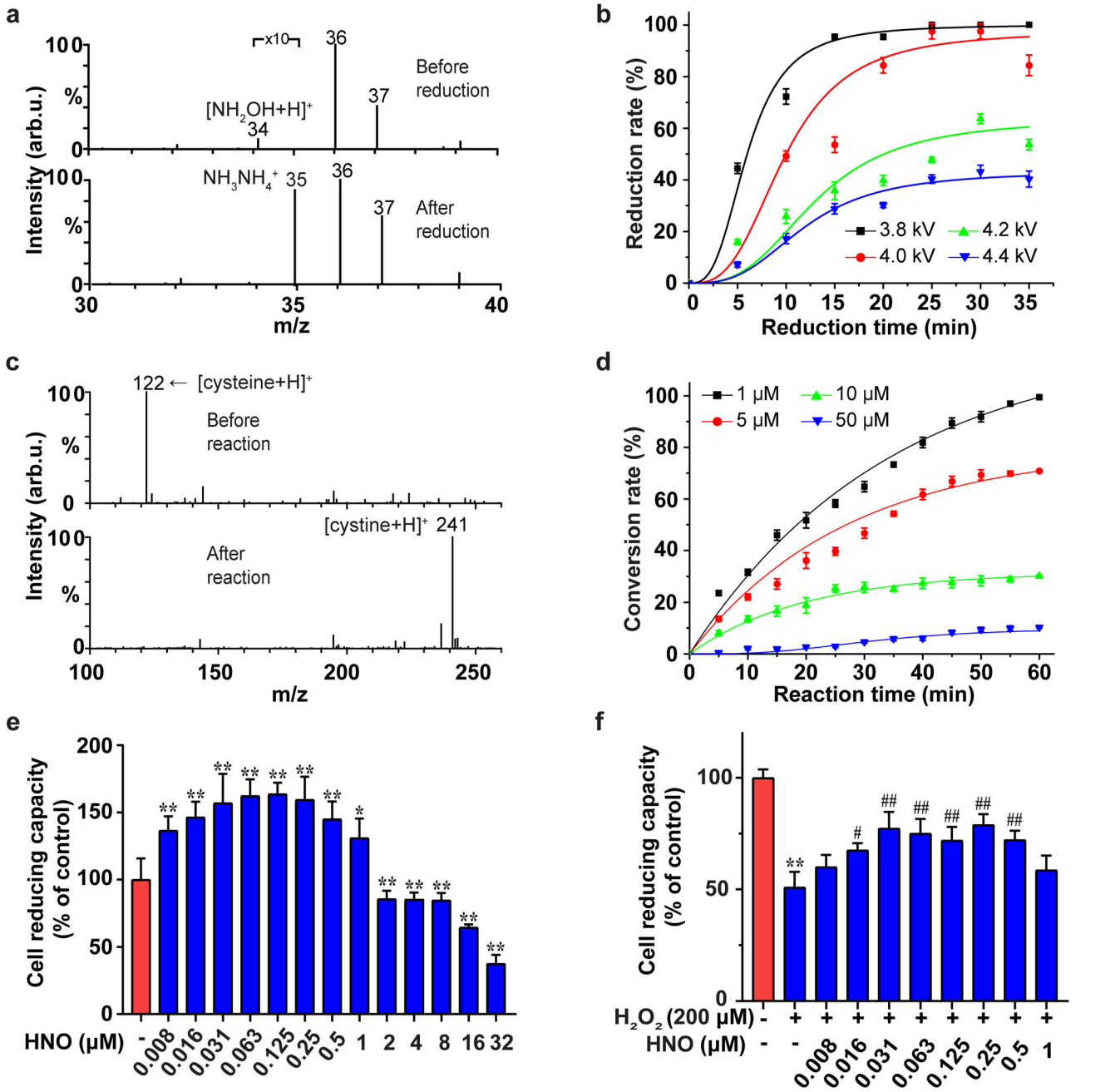

Fig. 4 | Further validation and application of the NH_2OH and HNO products of N_2 disproportionation with $(H_2O)_2^{+\cdot}$. **a** Electrolytic reduction of the collected NH_2OH product (corresponding signal at *m/z* 34) into NH_3 (corresponding signal at *m/z* 35) confirmed by mass spectrometry detection. The signals at *m/z* 36 and *m/z* 37 correspond to $(H_2O)_2^{+\cdot}$ and $H^+(H_2O)_2$. **b** The kinetics of electrolytic reduction of NH_2OH collected at different discharge voltages into NH_3 determined using the indophenol blue method[42] (see Supplementary Fig. 9). **c** The conversion of cysteine (corresponding signal at *m/z* 122) into cystine (corresponding signal at *m/z* 241) via the reaction of cysteine with the collected HNO product of the disproportionation reaction of N_2 confirmed by mass spectrometry detection. **d** The kinetics of cysteine conversion into cystine via the reaction with the collected HNO product (~25 μM; collection time 30 min) at different cysteine concentrations. **e** Effects of different concentration levels of HNO alone on HT22 cell reducing capacity. **f** HT22 cells were pretreated with different concentration levels of HNO for 24 h and incubated with or without H_2O_2 (200 μM) for 1 h. Cell reducing capacity as determined with Cell Counting Kit-8 assay. $^{*}P < 0.05$ and $^{**}P < 0.01$versus control, $^{\#}P < 0.05$ and $^{\#\#}P < 0{\cdot}01$ versus model. The error bars indicate the standard deviation ($n = 3$).

experiments with $^{15}N_2$ instead of $^{14}N_2$ displayed the characteristic $^{15}NH_2$ peak (Supplementary Fig. 8a).

Application of the reaction products

Note that both NH_2OH and HNO products of the disproportionation reaction between N_2 and $(H_2O)_2^{+\cdot}$ are highly valuable chemicals. Further, using a low-cost homemade setup powered by a 1.5 V solar cell battery (Supplementary Fig. 9) in our laboratory, we were able to easily reduce the prepared NH_2OH into NH_3 (Fig. 4a, Supplementary Fig. 9) with the conversion rate of almost 100% within ca. 30 min (Fig. 4b). The simplicity of the experimental assembly suggests that the disproportionation reaction between N_2 and $(H_2O)_2^{+\cdot}$ could probably serve the agricultural fields as tiny onsite ammonia plants, which could be powered by solar cells[31]. We also showed that the HNO product could be used to directly convert cysteine into cystine (Fig. 4c) with the conversion rate of almost 100% within ca. 60 min (Fig. 4d) under the

conditions tested. This observation suggests that HNO could be used for the specific chemical modification of thiols in proteins.

In model experiments, we demonstrated the potential utility of the collected HNO product in promoting the proliferation of HT22 cells and protecting them from H_2O_2-induced oxidative stress (Fig. 4e, f, Supplementary Fig. 10, Supplementary Fig. 11). While the low dose of HNO (0.008–1 μM) remarkably increased cell reducing capacity, as measured by Cell Counting Kit-8 (CCK-8), a high dose of HNO (1–32 μM) was found to inhibit cell reducing capacity (Fig. 4e, Supplementary Fig. 10). These observations suggest an important role of HNO in regulating cell growth[32]. It has been reported that HNO can interact with and modify several protein targets, such as thiol proteins, stimulating cell proliferation[33]. In addition to that, through the reaction with the dehydrogenase and tetrazolium salts, HNO could also convert to NO, which further regulates cell growth. Indeed, NO has been established as a potent modulator of cell proliferation and the cell cycle, including stimulatory and inhibitory effects[34,35]. We propose that the observed two-phased effect of HNO on cell reducing capacity could be attributed to a complex signaling pathway involving NO. Further investigation is required to clarify the effects of HNO on cell reducing capacity.

Characteristics of the N_2 disproportionation reaction

Using the total plate area (~ 3.5 × 5.5 cm^2) as the active area of the 76-pin device (Fig. 3a), we estimated the Faradic efficiency (FE) ≈ 64% with the yield ≈ 1.14 μg cm^{-2} h^{-1} for NH_2OH and the FE ≈ 20% with the yield ≈ 0.37 μg cm^{-2} h^{-1} for HNO (optimized in Supplementary Fig. 12). Note that the maximum yields calculated based only on the total effective surface area of 76 needle tips (as the plasma is activated only at the tip surface of the needles) were 5.10 × 10^3 μg cm^{-2} h^{-1} for NH_2OH and 1.53 × 10^3 μg cm^{-2} h^{-1} for HNO, respectively (see details in Supplementary Note 2). The lower yield and FE for HNO is probably caused by its higher reactivity, resulting in the partial conversion of HNO by H_2O and other chemicals in the collected solution. Thus, in MS (Supplementary Fig. 13a-d), ion chromatography (Supplementary Fig. 13e-f), and UV-Vis absorption spectroscopy (Supplementary Fig. 14) we also observed NO_3^-, NO_2^- and H_2O_2 products, which were likely produced by further conversion of the HNO product. The content of NO_3^-, NO_2^- and H_2O_2 produced over 10 min was estimated to be about 0.007 mM, 0.004 mM, and 0.03 mM, respectively. Interestingly, ion chromatography (Supplementary Fig. 15) and ^1H NMR spectroscopy (Supplementary Fig. 7b) data also indicated the production of NH_4^+ (about 0.02 mM over 10 min), which is likely through the reduction of NH_2OH product. The simple reduction of NH_2OH to NH_3 is demonstrated by the results in Fig. 4a. The origin of NH_3 via the reduction of N_2 by water plasma was further confirmed by isotope-labeling experiments (Supplementary Fig. 7b).

By integrating the calculated yields of N-containing products, the conversion rate of N_2 under the optimum conditions was estimated as ca. 0.001%, which is higher than in other plasma methods (for details see Supplementary Note 3)[36]. We believe that the higher conversion rate in our method is mainly due to the formation of abundant $(H_2O)_2^{+\bullet}$ cations, which act as efficient activators of N_2 molecule. As NH_2OH can be converted to NH_3 with nearly 100% efficiency, the estimated NH_3 production rate under the optimum conditions was ca. 1.8 μg cm^{-2} h^{-1} (for details see Supplementary Note 3).

In comparison with the HB process and other methods of N_2 fixation, including catalytic and plasma methods (Tables 1 and 2), our method offers considerably higher economy efficiency (1.54 $ kwh^{-1} for NH_2OH and 7310 $ kwh^{-1} for HNO), which is owing to the high value of NH_2OH and particularly HNO products as compared to NH_3. In terms of energy cost (g kwh^{-1}), our method is currently ca. 3 orders of magnitude less efficient than HB and ca. one to two orders of magnitude less efficient than plasma-based methods for N_2 fixation reported earlier (0.154 g kwh^{-1} for NH_2OH and 0.149 g kwh^{-1} for HNO). The higher energy cost in our method is mainly due to the avoidance of a catalyst, high pressures and high temperatures. The energy cost is expected to reduce as the plant continues to be upgraded. In comparison with several catalytic methods for N_2 fixation under mild conditions (near room temperature and atmospheric pressure) reported earlier, our method offers similar yield of N-containing products (1.14 μg·cm^{-2}·h^{-1} for NH_2OH and 0.37 μg·cm^{-2}·h^{-1} for HNO). The product yield of NH_2OH was ca. two times higher than that of NH_3, while the product yield of HNO was ca. three times lower than the integral product yield of NO_3^- and NO_2^- (Table 1). The lower yield of HNO compared to NO_3^- and NO_2^- probably reflects the high reactivity of HNO intermediate to give NO_3^- and NO_2^-. It is a challenge for further research to optimize the reaction parameters toward the higher yield and stability of the high-value HNO product.

Overall, key merits of our method include: (1) mild conditions; low cost; easy implementation; scalability; (2) high-value products: according to the current market, the potential value about 1.5 $ of NH_2OH and 7310 $ of HNO were produced by 1 kWh of electricity (≤0.2 $); (3) no catalyst needed; (4) high atom economy: the oxidation of one nitrogen atom of N_2 to HNO coupled with the simultaneous reduction of the other nitrogen atom of N_2 to NH_2OH.

In summary, we have demonstrated that the atmospheric N_2 can be disproportionately fixed by $(H_2O)_2^{+\bullet}$ under ambient conditions into economically valuable NH_2OH and HNO, presenting an alternative to the current necessity of fixing N_2 into NH_3. The combination of the essential N, O and H atoms in the obtained products considerably increases variability of possible chemistries as compared to NH_3. The experimental and theoretical studies indicate that triplet-state N_2 is activated by $(H_2O)_2^{+\bullet}$ to form intermediate $HONH\text{-}HNOH^{+\bullet}$, which is further decomposed to form $NH_2OH^{+\bullet}$ and HNO. The mechanism of N_2 fixation by the 2c-3e $(H_2O)_2^{+\bullet}$ structure through the excited-state double-proton transfer is principally different from the previously proposed methods. Remarkably, the formation of NH_2OH and HNO product occurs in the gas phase, which opens potentialities for their direct in-situ application, without the need of sample collection. The design ideas in this work could motivate more research efforts to further explore the potential of distinct $(H_2O)_2^{+\bullet}$ chemistry and open alternative possibilities for green nitrogen fixation.

Methods

Chemicals and material

NH_2OH•HCl, 8-quinolinol and 2-(diphenylphosphino) benzoic acid were purchased from Shanghai Sun Chemical Technology Co., Ltd (China), with a purity >99%. D_2O was purchased from Cambridge Isotope Laboratories, Inc. (Andover, MA, USA), with a purity >99%. Authentic Angeli's salt (AS) used in fluorescence quantification experiments was purchased from Cayman Chemical and stored at −20 °C, with a purity >99%. Ultra-purity N_2 (>99.999%), ultra-purity helium (>99.999%), ultra-purity argon (>99.999%) and ultra-purity $^{15}N_2$ (>99%) were obtained from Jiangxi Guoteng Gas Co. Ltd (Nanchang, China). Water used in all experiments was purified by a Milli-Q system (Millipore, USA).

Foetal bovine serum (FBS) was purchased from Zhejiang Sorfa Life Science Co., Ltd. (Zhejiang, China). Dulbecco's modified eagle's medium (DMEM), Trypsin-ethylene diamine tetraacetic acid solution and phosphate buffered saline (PBS) were obtained from Solarbio Life Science Co., Ltd. (Beijing, China). H_2O_2 (30%) was purchased from Xilong Scientific Co., Ltd. (Guangdong, China). The CCK-8 assay kit was obtained from Biosharp Life Sciences Co., Ltd. (Anhui, China). Microplate reader was purchased from Gene Company Limited (Hong Kong SAR, China). CO_2 incubator was obtained from SANYO (Osaka, Japan). Inverted microscope was purchased from Leica (Germany). Superclean bench was from Suzhou Purification Co., Ltd. (Shanghai, China).

Table 1 | Comparison with catalytic methods of nitrogen fixation under mild conditions

Method	Catalyst	Products	Conditions	Product yield ($\mu g \cdot cm^{-2} \cdot h^{-1}$)	Economy efficiency[a] $\$ cm^{-2} \cdot h^{-1}$	FE (%)	Ref
Electrocatalytic	MoS_2	NH_3	RT[b], AP[c]	5.39	0.3234×10^{-6}	1.17	44
Electrocatalytic	PEBCD/C	NH_3	RT, AP	1.58	0.0948×10^{-6}	2.85	45
Electrocatalytic	Au nanorods	NH_3	RT, AP	1.65	0.099×10^{-6}	3.88	46
Electrocatalytic	Ru/C	NH_3	20 °C, AP	0.21	0.0126×10^{-6}	0.28	47
Electrocatalytic	Pt/C	NH_3	RT, AP	69.77	4.1862×10^{-6}	0.52	48
Electrocatalytic	Fe_2O_3/CNTs	NH_3	20 °C, AP	0.22	0.0132×10^{-6}	0.15	49
Electrocatalytic	AuHNCs	NH_3	RT, AP	3.90	0.234×10^{-6}	30.2	50
Electrocatalytic	B-graphene	NH_3	RT, AP	9.80	0.588×10^{-6}	10.8	51
Photocatalytic	P3MeT/TiO_2	NH_3	20 °C	0.03	0.0018×10^{-6}	N/A	52
Photocatalytic	Au/black Si/Cr	NH_3	N/A	1.33	0.0798×10^{-6}	N/A	53
Photocatalytic	TiO_2/Au/a-TiO_2	NH_3	RT	0.23	0.0138×10^{-6}	N/A	54
Photocatalytic	Au NPs/Nb-$SrTiO_3$/Zr/ZrOx	NH_3	RT	0.01	0.0006×10^{-6}	N/A	55
Biological	Enzyme	NH_3	Antarctica	5.9×10^{-3}	N/A	N/A	56
Disproportionation by $(H_2O)_2^{+\cdot}$	No		RT, AP	1.14[d]	1.14×10^{-5}		This work
		NH_2OH		(5.10×10^3)[e]	0.051	64.0	
		HNO		0.37[d]	0.0555	18.0	
				(1.53×10^3)[e]	229.5		
		NH_3		0.63[d]	6.3×10^{-6}	55.0	
		NO_2^-		0.34[d]	0.07×10^{-6}	33.0	
		NO_3^-		0.81[d]	0.17×10^{-6}	96.0	

[a] Note that the economy efficiency for the catalytic methods does not account for the price of the catalyst. [b] RT: room temperature. [c] AP: atmospheric pressure.
[d] The $yield_{min}$, which is the yield obtained when the total surface area of the discharge needle array was accounted for. [e] The $yield_{max}$, which is the yield obtained when only the total effective surface area of the 76 needle tips was accounted for. In this work, the yield was given for NH_2OH product. The NH_2OH product could be converted into NH_3 with ca. 100% efficiency (Fig. 4b). N/A: Information not available in the article. For regarding the calculation of product yields see Supplementary Note 2.

Table 2 | Comparison with plasma methods of nitrogen fixation

Approach	Catalyst	Products	Energy cost MJ mol^{-1}	Energy yield g kwh^{-1}	Economy efficiency $\$ kwh^{-1}$	Ref
[a]DBD plasma	Copper wire	NH_3	18.5	3.308	0.1985	57
DBD plasma	Alumina medium	NH_3	33.4	1.832	0.1099	58
DBD plasma	ferroelectric materials	NH_3	68	0.900	0.0540	59
DBD plasma	Ru/Mg/Al_2O_3	NH_3	1.71	35.8	2.1474	60
DBD plasma	Ru/Al_2O_3	NH_3	32.4	1.9	0.1133	61
Non-thermal plasma	Ru/Cs/carbon nanotubes	NH_3	26.6	2.3	0.1380	62
Nonequilibrium plasma	No	NH_3	95	0.644	0.0387	36
Plasma-water droplet	No	NH_3	9500	0.006	0.0004	63
Plasma-activated nitrogen fixation	No	NH_3	0.61	100.3	6.0197	10
[b]UV irradiation plasma	No	NH_3	988	0.062	0.0037	64
Plasma electrolytic system	No	NH_3	139	0.440	0.0264	65
[c]DC plasma-driven electrolysis	No	NH_3	100	0.612	0.0367	66
		NO_3^-		2.232	0.0134	
DBD plasma	No	NO_3^-	8	27.90	0.1674	67
DBD plasma	No	NO_2^-	1175	0.141	0.0008	68
Disproportionation by $(H_2O)_2^{+\cdot}$	No	NH_2OH	770	0.154	1.5429	This work
		HNO	2290	0.049	7310.0	
		NH_3	504	0.121	0.007	
		NO_2^-	2535	0.065	0.01	
		NO_3^-	1488	0.155	0.03	

[a] DBD: dielectric barrier discharge. [b] UV: ultraviolet. [c] DC: direct current. For Details regarding the calculation of energy cost see Supplementary Note 4.

A coumarin-based fluorescent probe, P-CM, was synthesized in our lab according to the method reported by Tan et al with modification, with a purity >99%[30]. In detail, 2-(diphenylphosphino) benzoic acid (306 mg, 1 mmol) was dissolved in 50 mL of anhydrous CH_2Cl_2 under inert atmosphere. Then, 4-(dimethylamino) pyridine (6.1 mg, 0.05 mmol) and 1-ethyl-3-(3-dimethylaminopropyl) carbodiimide hydrochloride (191.7 mg, 1 mmol) were added, and the reaction mixture was stirred at room temperature for 30 min. 7-Hydroxycoumarin (194.6 mg, 1.2 mmol) was then added, and the resulting mixture was stirred at room temperature. The reaction mixture was concentrated under reduced pressure. The residue was purified by the silica gel chromatography (ethyl acetate/ petroleum ether = 1:2, v/v) to yield P-CM product as a faint yellow solid (423 mg, 0.93 mmol). The isolated mass and yield were calculated to be ~423 mg and 93%, respectively. Even though the reaction was conducted at room temperature, it is essential to note that some reagents, such as petroleum ether, are highly volatile. Hence, in order to ensure the safety of experiments, appropriate control safeguards are needed to prevent potential hazards. ^{1}H NMR ($CDCl_3$, 500 MHz) δ(ppm): 8.278–8.245 (m, 1H), 7.681–7.657 (d, J = 9.6 Hz, 1H), 7.502–7.474 (m, 2H), 7.440–7.418 (m, 1H), 7.377–7.277 (m, 10H), 7.022–6.989 (m, 1H), 6.930–6.902 (m, 2H), 6.396–6.372 (d, J = 9.6 Hz, 1H). MS (ESI) *m/z* 451.0 $[M + H]^+$ (Fig. 3f).

Reaction between N_2 and $(H_2O)_2^{+\bullet}$ with real-time MS

Experimental setup to study the products of the reaction between N_2 and $(H_2O)_2^{+\bullet}$ in real time is shown in Fig. 1a. In order to produce $(H_2O)_2^{+\bullet}$, neutral Ar gas was bubbled through liquid H_2O at a flow rate of 10 ~ 100 mL min^{-1}, and the produced H_2O/Ar vapor was guided to the home-made ambient corona discharge ion source through Teflon tubing with inner diameter (ID) of 0.75 mm. To build the ion source, a sharp stainless-steel needle (outer diameter (OD) 150 μm; end curvature radius ~30 μm) was used as the discharge electrode for plasma. The needle was coaxially inserted into a fused silica capillary (ID 0.25 mm, OD 0.40 mm) and was fixed coaxially with a union tee and silica ferrule. The back end of the tee was connected to the H_2O/Ar line. The distance from the inlet of the mass spectrometer capillary to the tip of the ion source was 20 mm. The direct current (DC) voltage of +2.0 kV was applied to the stainless-steel needle in order to generate ambient corona discharge. A flow of neutral N_2 (100 mL min^{-1}) was introduced through a separate channel to interact with the produced $(H_2O)_2^{+\bullet}$. In a reference experiment, N_2 was replaced by Ar (Supplementary Fig. 1a).

Scale-up reaction between N_2 and $(H_2O)_2^{+\bullet}$

The experimental setup for the scaled-up disproportionation reaction between N_2 and $(H_2O)_2^{+\bullet}$ with the collection of reaction products is presented in Fig. 3a. High-purity N_2 (99.999 %) controlled by mass flow controller was bubbled through liquid H_2O and was then transferred through the discharge reactor in quartz enclosure toward the outlet tubing connected with a collection bottle. The reactor consisted of a discharge array of 76 tungsten needles under DC voltage (anode) and a flat grounded electrode (cathode). The distance between the tips of two adjacent needles was evenly set as 0.5 cm. The 76 anodes of the array were connected to the same positive terminal of the DC high voltage power. Cationic reaction product $NH_2OH^{+\bullet}$ was collected by an indium tin oxide (ITO) coated glass bottle filled with 8-quinolinol probe solution (6 mL), which was placed on the top of the cathode. Neutral reaction product HNO was pumped out through the outlet line into the bottle filled with P-CM probe solution (2 mL) (Fig. 3a). The amount of electric charge neutralized on the cathode plate was determined by an electrochemical workstation (Shanghai Chenhua Instrument Co., Lt, CHI660E).

MS settings

MS detection was carried out using an LTQ-XL ion trap mass spectrometer (LTQ-XL, Thermo Scientific, San Jose, CA, USA). The temperature of the ion transfer capillary was 150 °C. The capillary voltage was 1.0 V. The tube lens voltage was 30.0 V. The pressure of ion trap was 1×10^{-5} torr. High-purity helium (99.999%) was used as the collision gas. The CID-MS experiments were performed by applying excitation alternating current voltage to the end caps of the ion trap to induce collisions of the isolated ions. The CID-MS spectra were obtained by activation of the precursor ions at the normalized collision energy varied from 0% to 50%. Ion detection was done in the positive ion mode. Other LTQ-XL parameters were automatically optimized by the system.

Quantification of NH_2OH by UV-Vis spectroscopy

The concentration of collected NH_2OH was determined by the 8-quinolinol color test method with modification[29]. In detail, 1.2 mL phosphate buffer (0.05 M, pH 6.8), 0.24 mL trichloroacetic acid solution and 1.2 mL sodium carbonate solution (1.0 M) were mixed in a tube. Then 1.2 mL ethanol solution of 8-quinolinol (10 mg mL^{-1}) was added. Finally, pure water was added into the tube to bring the solution volume to 6 mL. Thus prepared 6 mL reagent solution was placed on top of the cathode plate. The N_2 disproportionation reaction was then started. The UV-Vis absorption spectra of the solution were measured at different reaction times (0, 5, 10, 20, 30, 40 min) on a spectrophotometer (UV-1900i, Shimadzu, Japan). The formation of indooxine due to the reaction between NH_2OH and 8-quinolinol was evident by the characteristic absorbance band with the maximum at 705 nm. For calibration, UV-Vis spectra were collected for a series of blank (zero time of disproportionation reaction) reagent solutions spiked with different concentrations of NH_2OH (0.01 mM, 0.05 mM, 0.1 mM, 0.2 mM, 0.25 mM), showing good linear correlation of indooxine absorbance with NH_2OH concentration by three independent measurements (Supplementary Fig. 5a, b). Blank UV-Vis measurements were also done when no NH_2OH was added.

Infrared and Raman spectroscopy

The collected samples and NH_2OH•HCl standard were analyzed on a Thermo Nicolet iS5 Fourier transform infrared spectrograph. In detail, KBr samples were powdered and spread evenly on top of the cathode plate (Fig. 3a). The N_2 disproportionation reaction was then run over 24 h. The sample collected on the cathode plate was analyzed by infrared spectroscopy. NH_2OH•HCl sample was measured for control.

The collected samples and NH_2OH•HCl standard were also analyzed by Via RM2000 laser Raman spectroscopy (Renishaw company, United Kingdom) with 10 s integration time in the spectral range of 400–4000 cm^{-1}. Continuous-Wave laser irradiation at the wavelength of 532 nm was focused through a 50X objective to excite the samples. Deionized water was placed on top of the cathode plate (Fig. 3a). The N_2 disproportionation reaction was run over 48 h. The product collected on the cathode plate was analyzed by Raman spectroscopy. The authentic NH_2OH•HCl solution was analyzed for control.

Quantification of HNO by fluorescence spectroscopy

The amount of collected HNO was estimated by the method reported by Tan et al[30]. P-CM probe was freshly dissolved in *N,N*-dimethylformamide to obtain 1 mM stock solution, which was diluted to 10 μM with 100 mM PBS buffer (pH 7.4). The prepared P-CM solutions (10 μM, total volume = 2 mL) were connected to the reactor outlet line as shown in Fig. 3a for different periods of reaction time at room temperature. The fluorescence of 7-hydroxycoumarin formed through the reaction of HNO with the P-CM probe was excited at 370 nm and was measured at 450 nm. Fluorescence from the blank P-CM (10 μM) solution (not reacted with HNO) was measured as control. The yields of HNO were calculated from a standard curve using AS as HNO source. A stock solution of AS (2 μM mL^{-1}) was prepared in 1 M NaOH solution and stored at −20 °C. 20 μL AS standard solutions with different concentrations (0.01 μM, 0.25 μM, 1 μM, 2 μM, 5 μM) were separately

added into 10 μM P-CM solutions to bring the volume to 2 mL. Then, fluorescence spectra were recorded. The fitting curve showed good linearity of fluorescence intensity at 450 nm with HNO concentration by three independent measurements (Supplementary Fig. 5c, d).

Noteworthy, while HNO is known to dimerize at high concentrations[37], the collected HNO solutions displayed considerable stability over the period of at least 2 days (Supplementary Fig. 11). The stability of HNO product is due to its relatively low concentration (sub mM), which prevents significant dimerization of HNO in the collected solution. Our observations are consistent with the recent reports indicating long-term stability of HNO in aqueous solutions under physiologically relevant conditions[38,39].

Ion chromatography

The amounts of NH_3, NO_3^- and NO_2^- formed over the interaction between water plasma and N_2 were also estimated by ion chromatography (Thermo-Fisher DIONEX ICS-1100). The test procedure followed the standard operation procedure provided by the vendor. Briefly, 25 μL of the resultant was injected into the chamber for separation. Delivery speed was 4 mL min^{-1}. The peak eluted at the retention time of 9 min was assigned to NH_4^+. The amount of NH_4^+ was estimated using a calibration curve by standard solutions (Supplementary Fig. 15). The peaks eluted at the retention time of 5 min and 8 min were assigned to NO_2^- and NO_3^-. The amounts of NO_2^- and NO_3^- were estimated using a series of standard solutions (Supplementary Fig. 13e, f).

Quantification of H_2O_2 by UV-Vis spectroscopy

The amount of H_2O_2 was measured by UV-Vis absorption spectroscopy (UV-1900i, Shimadzu, Japan). According to reference[40], potassium permanganate was reduced by hydrogen peroxide in sulfuric acid with the maximum absorption peak at 525 nm. The amount of H_2O_2 was derived from the amount of consumed MnO_4^- for calibration with a series of standard solutions (Supplementary Fig. 14).

Experiments on HT22 cells treated with HNO product

It was reported that H_2O_2 signaling via thiol modification may lead to radical-mediated cellular damage (i.e., lipid peroxidation, protein carbonyl formation, etc.) due to the Fenton reaction[33]. In contrast, HNO demonstrates the ability to provide neuroprotection, and inhibit deleterious radical chain reaction, oxidative stress and lipid peroxidation[41]. Thus, HNO could interact with thiols thereby reducing the toxic effect of H_2O_2. In order to explore the possibility of using HNO to protect cells against H_2O_2 toxicity, we incubated HT22 cells with HNO and then treated them with H_2O_2.

In the present experiments, we established H_2O_2-induced oxidative stress models in HT22 cells to investigate whether HNO has antioxidative stress and neuroprotective effects. HNO was generated using the disproportionation reaction of N_2 with $(H_2O)_2^{+\bullet}$ under ambient conditions. HT22 cells were purchased from Procell Life Science & Technology Co., Ltd. and cultured in DMEM supplemented with 10% (v/v) FBS and 1% penicillin/streptomycin at 37 °C with the atmosphere of 5% CO_2. To induce cell damage, H_2O_2 was added to the culture for 1 h.

The HT22 cells were seeded in 96-well plates (0.8×10^5 cells/well) and incubated with different concentrations of HNO for 24 h followed by H_2O_2 treatment. Cell reducing capacity was examined by the CCK-8 assay kit (Dojindo, Tokyo, Japan). The absorbance of the samples was measured at 450 nm by microplate reader. The cell survival ratio was expressed as the percentage of the control.

All of the statistical analyses were performed by the SPSS 21.0 software. All of the data are expressed as the mean ± SD. Comparison between the two groups was assessed with an unpaired *t*-test, while comparison among several groups was evaluated using one-way ANOVA. The *p*-value <0.05 was considered statistically significant.

Calculation of the Faradaic efficiency and yield

For the experiment setup shown in Fig. 3a, the yields of NH_2OH and HNO were calculated using the following equations reported in earlier literature[42]:

$$\text{Yield}_{NH2OH} = (C_{NH2OH} \times V_{NH2OH} \times M_{NH2OH})/(t \times S) \quad (1)$$

$$\text{Yield}_{HNO} = (C_{HNO} \times V_{HNO} \times M_{HNO})/(t \times S) \quad (2)$$

where V is the volume of absorption solution (V_{NH2OH} = 6 mL; V_{HNO} = 2 mL), t is the reaction time (10 min), C is the concentration of the collected product over 10 min (*e.g.*, at 4.2 kV: C_{NH2OH} = 18.5 μM and C_{HNO} = 17.7 μM, determined using calibration curves in Supplementary Fig. 5), M is the molar mass of a collected product (M_{NH2OH} = 33 g mol^{-1}; M_{HNO} = 31 g mol^{-1}), S is the total effective surface area to conduct the reaction. The S value is measured by microscope (For details see Supplementary Note 2).

The FE for N_2 reduction was determined as the amount of electric charge used for the generation of NH_2OH divided by the total charge passed through the cathode electrode during reaction. The FE for N_2 oxidation was determined as the amount of electric charge used for the generation of HNO divided by the total charge passed through the electrodes during reaction. Assuming that one electron is needed to produce one HNO molecule and one NH_2OH molecule (Fig. 2a), the FE value was calculated according to the reference reported by Wang et al[42]:

$$FE = (n \times F \times C \times V)/Q \quad (3)$$

where n is the number of electrons transferred in the reaction (n = 1 in our case); F is the Faraday's constant (F = 96485.33 C mol^{-1}); C is the concentration of the collected NH_2OH or HNO; V is the volume of absorption solution to collect NH_2OH or HNO; and Q denotes the total charge passed through the cathode electrode during reaction (0.0168 C over 10 min reaction at 4.2 kV).

Reduction of NH_2OH to NH_3

To quantify the amount of NH_2OH collected during N_2 disproportionation reaction, the NH_2OH product of N_2 disproportionation reaction was collected into an ITO coated glass bottle filled with the solution of 8-quinolinol probe (Fig. 3a) for 30 min. The concentration of indooxine produced through the reaction between NH_2OH and 8-quinolinol was quantified by UV-Vis experiments (Supplementary Fig. 5a), and the concentration of collected NH_2OH was derived accordingly. Then, under the exactly identical conditions, the NH_2OH product of N_2 disproportionation reaction was collected into an ITO coated glass bottle filled with deionized water (without 8-quinolinol). The solution containing NH_2OH was transferred into a cell for electrochemical reduction, which was powered by a 1.5 V solar cell battery (Supplementary Fig. 9). The positive and negative electrodes (diameter 0.5 mm) connected to the 1.5 V battery were immersed into the solution to a depth of 1 cm for 35 min. The formation of NH_3 was confirmed by MS analysis (Fig. 4a). The concentration of generated NH_3 was spectrophotometrically determined using the indophenol blue method[43]. In detail, a 1 mL of the solution from the electrochemical reduction bottle was transferred into a 15 mL centrifuge tube. Then, 9 mL of 0.005 mol L^{-1} sulfuric acid aqueous solution, 0.5 mL of 50 g L^{-1} salicylic acid solution containing 50 g L^{-1} sodium citrate and 2 mol L^{-1} NaOH solution, 0.1 mL of 0.05 mol L^{-1} NaClO and 0.1 mL of 10 g L^{-1} $Na_2[Fe(NO)(CN)_5]\cdot 2H_2O$ were added into the tube and mixed. After 1 h, the absorption spectrum was measured using UV-Vis spectrophotometer (Supplementary Fig. 9). The formation of indophenol blue product was determined by measuring the absorbance at 705 nm. The calibration of the method was achieved using

ammonium chloride solutions of known concentration as standards. The concentration of NH_3 was derived from the calibration curve (Supplementary Fig. 9).

Reaction of HNO with cysteine

The reaction of HNO with cysteine was investigated using the setup shown in Fig. 3a. The experiment was done under the same conditions as in Fig. 3a, with the exception that the P-CM probe solution in the collection bottle was replaced with cysteine solution at different concentrations (1–50 μM). Cystine produced by the reaction between HNO and non-reacted cysteine were detected by MS analysis (Fig. 4c).

Theoretical calculations

Theoretical calculations were performed using the Gaussian 16 electronic structure programs and ORCA quantum chemistry program package (v5.0.4). The geometries of reactants, intermediates and products were optimized with B2GP-PLYP density functional with quadruple basis set. The same functional was used for vibrational analysis and the Gibbs free energy estimation at 298 K. This virtual orbital-dependent density functional theory method was chosen based on its performance on a set of small, related molecules with available experimental or high-level electronic structure data—namely N_2, NO, HNO and $(H_2O)_2^+$. Final electronic energies were calculated at CCSD(T)/CBS level with an expected accuracy of <1 kcal mol^{-1} (0.04 eV) for single-reference molecular systems. Multi-reference character of the proposed TS state (Fig. 2b), supported by fractional occupation number weighted electron density analysis (Supplementary Fig. 3), precludes us from drawing a precise conclusion about its position on the energy diagram. Consistent with the results of numerous recent benchmark studies, a difference of ≈0.10 eV was observed between CCSD(T)/CBS and B2GP-PLYP/aug-cc-pVQZ data with the exception of $(H_2O)_2^+$ conformations. See Supporting Information for details and references.

Reporting summary

Further information on research design is available in the Nature Portfolio Reporting Summary linked to this article.

Data availability

The authors declare that all the data that supports the findings of the study are included in the main text and Supplementary Information Files. The source data are available from the corresponding authors on request. All the data generated in this study have been deposited in the Figshare database under [https://doi.org/10.6084/m9.figshare.25028042]. Source data are provided with this paper.

References

1. Yeung, L. Y. et al. Extreme enrichment in atmospheric $^{15}N^{15}N$. *Sci. Adv.* **3**, 6741 (2017).
2. Legare, M. A. et al. Nitrogen fixation and reduction at boron. *Science* **359**, 896–899 (2018).
3. Hoffman, B. M., Lukoyanov, D., Yang, Z.-Y., Dean, D. R. & Seefeldt, L. C. Mechanism of nitrogen fixation by nitrogenase: the next stage. *Chem. Rev.* **114**, 4041–4062 (2014).
4. Chen, J. G. et al. Beyond fossil fuel–driven nitrogen transformations. *Science* **360**, aar6611 (2018).
5. Tanabe, Y. & Nishibayashi, Y. Comprehensive insights into synthetic nitrogen fixation assisted by molecular catalysts under ambient or mild conditions. *Chem. Soc. Rev.* **50**, 5201–5242 (2021).
6. Li, J. et al. Fundamentals and advances in emerging crystalline porous materials for photocatalytic and electrocatalytic nitrogen fixation. *ACS Appl. Energy Mater.* **5**, 9241–9265 (2022).
7. Fang, Y. et al. Graphdiyne interface engineering: highly active and selective ammonia synthesis. *Angew. Chem. Int. Ed.* **59**, 13021–13027 (2020).
8. Vu, M.-H., Sakar, M., Hassanzadeh-Tabrizi, S. A. & Do, T.-O. Photo(-electro)catalytic nitrogen fixation: problems and possibilities. *Adv. Mater. Interfaces* **6**, 1900091 (2019).
9. Soumare, A. et al. Exploiting biological nitrogen fixation: a route towards a sustainable agriculture. *Plants* **9**, 1011 (2020).
10. Winter, L. R. & Chen, J. G. N_2 fixation by plasma-activated processes. *Joule* **5**, 300–315 (2021).
11. Martín, A. J., Shinagawa, T. & Pérez-Ramírez, J. Electrocatalytic reduction of nitrogen: from Haber-Bosch to ammonia artificial leaf. *Chem* **5**, 263–283 (2019).
12. Huang, Z., Xiao, A., Liu, D., Lu, X. & Ostrikov, K. Plasma-water-based nitrogen fixation: status, mechanisms, and opportunities. *Plasma Process. Polym.* **19**, 2100198 (2022).
13. Wang, Q., Guo, J. & Chen, P. The impact of alkali and alkaline earth metals on green ammonia synthesis. *Chem* **7**, 3203–3220 (2021).
14. Li, L. et al. Reduction of dinitrogen via 2,3′-bipyridine-mediated tetraboration. *J. Am. Chem. Soc.* **142**, 6244–6250 (2020).
15. Kirkici, H., Bruno, D., Preiss, J. & Schaefer, G. Charge-transfer collisions between He_2^+ ions and N_2: branching ratio into vibrational states. *J. Appl. Phys.* **67**, 6041–6044 (1990).
16. Ristić, M. M., Aoneas, M. M., Vojnović, M. M. & Poparić, G. B. Excitation of electronic states of N_2 in radio-frequency electric field by electron impact. *Plasma Chem. Plasma Process.* **37**, 1431–1443 (2017).
17. Wang, M. et al. Abundant production of reactive water radical cations under ambient conditions. *CCS Chem.* **3**, 3559–3566 (2022).
18. Zhang, X., Ren, X., Zhong, Y., Chingin, K. & Chen, H. Rapid and sensitive detection of acetone in exhaled breath through the ambient reaction with water radical cations. *Analyst* **146**, 5037–5044 (2021).
19. Mi, D. et al. Generation of phenol and molecular hydrogen through catalyst-free C-H activation of benzene by water radical cations. *J. Am. Soc. Mass Spectrom.* **33**, 68–73 (2022).
20. Zhang, X. et al. Mass spectrometry distinguishing C=C location and cis/trans isomers: a strategy initiated by water radical cations. *Anal. Chim. Acta* **1139**, 146–154 (2020).
21. Yang, W. et al. Determination of C=C positions of unsaturated fatty acids in foods via ambient reactive desorption Ionization with water dimer radical cations. *J. Agric. Food. Chem.* **72**, 845–856 (2024).
22. Xiang, R. et al. Electrocatalytic synthesis of pyridine oximes using in situ generated NH_2OH from NO species on nanofiber membranes derived from NH_2-MIL-53(Al). *Angew. Chem. Int. Ed.* **62**, e202312239 (2023).
23. Shoman, E. M. & Aly, M. O. Nitroxyl (HNO): a possible strategy for fighting cancer. *Curr. Top. Med. Chem.* **16**, 2464–2470 (2016).
24. Irvine, J. C. et al. Nitroxyl (HNO): the cinderella of the nitric oxide story. *Trends Pharmacol. Sci.* **29**, 601–608 (2008).
25. Xing, D. et al. Capture of hydroxyl radicals by hydronium cations in water microdroplets. *Angew. Chem. Int. Ed.* **61**, e202207587 (2022).
26. Qiu, L., Morato, N. M., Huang, K.-H. & Cooks, R. G. Spontaneous water radical cation oxidation at double bonds in microdroplets. *Front. Chem.* **10**, 903774 (2022).
27. Sharpe, S. W. & Johnson, P. M. Triplet Rydberg states in molecular nitrogen. *J. Chem. Phys.* **85**, 4943–4948 (1986).
28. Yao, Y., Wang, H., Yuan, X.-Z., Li, H. & Shao, M. Electrochemical nitrogen reduction reaction on ruthenium. *ACS Energy Lett.* **4**, 1336–1341 (2019).
29. Frear, D. S. & Burrell, R. C. Spectrophotometric method for determining hydroxylamine reductase activity in higher plants. *Anal. Chem.* **27**, 1664–1665 (1955).
30. Mao, G.-J. et al. A highly sensitive and reductant-resistant fluorescent probe for nitroxyl in aqueous solution and serum. *Chem. Commun.* **50**, 5790–5792 (2014).

31. Du, Z., Denkenberger, D. & Pearce, J. M. Solar photovoltaic powered on-site ammonia production for nitrogen fertilization. *Sol. Energy* **122**, 562–568 (2015).
32. Lv, X. et al. Design and tuning of ionic liquid–based HNO donor through intramolecular hydrogen bond for efficient inhibition of tumor growth. *Sci. Adv.* **6**, eabb7788 (2020).
33. Bianco, C. L., Toscano, J. P., Bartberger, M. D. & Fukuto, J. M. The chemical biology of HNO signaling. *Arch. Biochem. Biophys.* **617**, 129–136 (2017).
34. Sciorati, C., Nisticò, G., Meldolesi, J. & Clementi, E. Nitric oxide effects on cell growth: GMP-dependent stimulation of the AP-1 transcription complex and cyclic GMP-independent slowing of cell cycling. *Brit. J. Pharmacol.* **122**, 687–697 (1997).
35. Wingrove, J. A. & O'Farrell, P. H. Nitric oxide contributes to behavioral, cellular and developmental responses to low oxygen in Drosophila. *Cell* **98**, 105–114 (1999).
36. Gorbanev, Y., Vervloessem, E., Nikiforov, A. & Bogaerts, A. Nitrogen fixation with water vapor by nonequilibrium plasma: toward sustainable ammonia production. *ACS Sustain. Chem. Eng.* **8**, 2996–3004 (2020).
37. Bartberger, M. D., Fukuto, J. M. & Houk, K. N. On the acidity and reactivity of HNO in aqueous solution and biological systems. *Proc. Natl. Acad. Sci. USA* **98**, 2194–2198 (2001).
38. Fehling, C. & Friedrichs, G. Dimerization of HNO in aqueous solution: an interplay of solvation effects, fast acid–base equilibria, and intramolecular hydrogen bonding? *J. Am. Chem. Soc.* **133**, 17912–17922 (2011).
39. Dobmeier, K. P., Riccio, D. A. & Schoenfisch, M. H. Xerogel optical sensor films for quantitative detection of nitroxyl. *Anal. Chem.* **80**, 1247–1254 (2008).
40. Chen, E. et al. High surface area N/O co-doped carbon materials: selective electrocatalysts for O_2 reduction to H_2O_2. *Catal. Today* **356**, 132–140 (2020).
41. Lopez, B. E., Shinyashiki, M., Han, T. H. & Fukuto, J. M. Antioxidant actions of nitroxyl (HNO). *Free Radical Biol. Med.* **42**, 482–491 (2007).
42. Wang, X. et al. Atomically dispersed Au1 catalyst towards efficient electrochemical synthesis of ammonia. *Sci. Bull.* **63**, 1246–1253 (2018).
43. Zhu, D., Zhang, L., Ruther, R. E. & Hamers, R. J. Photo-illuminated diamond as a solid-state source of solvated electrons in water for nitrogen reduction. *Nat. Mater.* **12**, 836–841 (2013).
44. Zhang, L. et al. Electrochemical ammonia synthesis via nitrogen reduction reaction on a MoS_2 catalyst: theoretical and experimental studies. *Adv. Mater.* **30**, 1800191 (2018).
45. Chen, G.-F. et al. Ammonia electrosynthesis with high selectivity under ambient conditions via a Li^+ incorporation strategy. *J. Am. Chem. Soc.* **139**, 9771–9774 (2017).
46. Bao, D. et al. Electrochemical reduction of N_2 under ambient conditions for artificial N_2 fixation and renewable eenergy storage using N_2/NH_3 cycle. *Adv. Mater.* **29**, 1604799 (2017).
47. Kordali, V., Kyriacou, G. & Lambrou, C. Electrochemical synthesis of ammonia at atmospheric pressure and low temperature in a solid polymer electrolyte cell. *Chem. Commun.* **17**, 1673–1674 (2000).
48. Lan, R., Irvine, J. T. S. & Tao, S. Synthesis of ammonia directly from air and water at ambient temperature and pressure. *Sci. Rep.* **3**, 1145 (2013).
49. Chen, S. et al. Electrocatalytic synthesis of ammonia at room temperature and atmospheric pressure from water and nitrogen on a carbon-nanotube-based electrocatalyst. *Angew. Chem. Int. Ed.* **56**, 2699–2703 (2017).
50. Nazemi, M., Panikkanvalappil, S. R. & El-Sayed, M. A. Enhancing the rate of electrochemical nitrogen reduction reaction for ammonia synthesis under ambient conditions using hollow gold nanocages. *Nano Energy.* **49**, 316–323 (2018).
51. Yu, X. et al. Boron-doped graphene for electrocatalytic N_2 reduction. *Joule* **2**, 1610–1622 (2018).
52. Hoshino, K., Kuchii, R. & Ogawa, T. Dinitrogen photofixation properties of different titanium oxides in conducting polymer/titanium oxide hybrid systems. *Appl. Catal. B-Environ.* **79**, 81–88 (2008).
53. Ali, M. et al. Nanostructured photoelectrochemical solar cell for nitrogen reduction using plasmon-enhanced black silicon. *Nat. commun.* **7**, 11335 (2016).
54. Li, C. et al. Promoted fixation of molecular nitrogen with surface oxygen vacancies on plasmon-enhanced TiO_2 photoelectrodes. *Angew. Chem. Int. Ed.* **57**, 5278–5282 (2018).
55. Oshikiri, T., Ueno, K. & Misawa, H. Selective dinitrogen conversion to ammonia using water and visible light through plasmon-induced charge separation. *Angew. Chem. Int. Ed.* **55**, 3942–3946 (2016).
56. Shiozaki, T. et al. Biological nitrogen fixation detected under Antarctic sea ice. *Nat. Geosci.* **13**, 729–732 (2020).
57. Aihara, K. et al. Remarkable catalysis of a wool-like copper electrode for NH_3 synthesis from N_2 and H_2 in non-thermal atmospheric plasma. *Chem. Commun.* **52**, 13560–13563 (2016).
58. Mindong, B., Zhitao, Z., Xiyao, B., Mindi, B. & Wang, N. Plasma synthesis of ammonia with a microgap dielectric barrier discharge at ambient pressure. *IEEE T. Plasma Sci.* **31**, 1285–1291 (2003).
59. Gómez-Ramírez, A., Cotrino, J., Lambert, R. M. & González-Elipe, A. R. Efficient synthesis of ammonia from N_2 and H_2 alone in a ferroelectric packed-bed DBD reactor. *Plasma Sources Sci. Technol.* **24**, 065011 (2015).
60. Kim, H.-H., Teramoto, Y., Ogata, A., Takagi, H. & Nanba, T. Atmospheric-pressure nonthermal plasma synthesis of ammonia over ruthenium catalysts. *Plasma Process. Polym.* **14**, 1600157 (2017).
61. Li, S., van Raak, T. & Gallucci, F. Investigating the operation parameters for ammonia synthesis in dielectric barrier discharge reactors. *J. Phys. D.* **53**, 014008 (2020).
62. Peng, P. et al. Atmospheric pressure ammonia synthesis using nonthermal plasma assisted catalysis. *Plasma Chem. Plasma Process.* **36**, 1201–1210 (2016).
63. Toth, J. R., Abuyazid, N. H., Lacks, D. J., Renner, J. N. & Sankaran, R. M. A plasma-water droplet reactor for process-intensified, continuous nitrogen fixation at atmospheric pressure. *Acs Sustain. Chem. Eng.* **8**, 14845–14854 (2020).
64. Haruyama, T. et al. Non-catalyzed one-step synthesis of ammonia from atmospheric air and water. *Green Chem.* **18**, 4536–4541 (2016).
65. Hawtof, R. et al. Catalyst-free, highly selective synthesis of ammonia from nitrogen and water by a plasma electrolytic system. *Sci. Adv.* **5**, eaat5778 (2019).
66. Pattyn, C. et al. Disproportionation of nitrogen induced by DC plasma-driven electrolysis in a nitrogen atmosphere. *Green Chem.* **24**, 7100–7112 (2022).
67. Dinh, D. K., Muzammil, I., Kang, W. S., Kim, D. & Lee, D. H. Reducing energy cost of in situ nitrogen fixation in water using an arc-DBD combination. *Plasma Sources Sci. Technol.* **30**, 055020 (2021).
68. Subramanian, P. S. G. et al. Plasma-activated water from DBD as a source of nitrogen for agriculture: specific energy and stability studies. *J. Appl. Phys.* **129**, 093303 (2021).

Acknowledgements

The authors acknowledge Dr. Lili Sun for preliminary calculations. The authors also thank Ms. Xuejiao Chen and Mr. Yuan Zhong for their help in performing the MS experiments. The authors are particularly grateful for the proof reading of the manuscript by Prof. Yinquan Wang. The work was supported by National Natural Science Foundation of China (21520102007, 22104014, 22364002, 22164002) (H.C., Xin.Z., and Xia.Z.), Jiangxi Provincial Natural Science Foundation (20232BAB213047) (Xia.Z.), Jiangxi Province International Cooperation

Project (20203BDH80W010, 20232BBH80012) (H.C.), and Jiangxi University of Chinese Medicine School-level Science and Technology Innovation Team Development Program (CXTD22005, 2004-5252300403). (H.C.).

Author contributions

H.C. independently developed the idea of the research, supervised the project and prepared the manuscript. Xia.Z. collected the MS data, interpreted the MS data, and co-wrote the manuscript draft. K.C., Xin.Z., W.Z., R.B., and H.C. edited the manuscript. L.H., J.W., W.Z and H.C. designed and conducted the HT22 cells experiments, collected and analyzed the data. Xin.Z., J.L., W.Y., R.S., K.H., S.F., and Xia.Z. collected the UV-Vis, fluorescence spectroscopy, Infrared, Raman and NMR data. R.B. conducted all the calculations.

Competing interests

The authors declare no competing interests.

Additional information

Supplementary information The online version contains supplementary material available at https://doi.org/10.1038/s41467-024-45832-9.

Correspondence and requests for materials should be addressed to Huanwen Chen.

Peer review information *Nature Communications* thanks Xiang-Rong Chen and the other, anonymous, reviewers for their contribution to the peer review of this work. A peer review file is available.